

Article

Characterization of the Microstructure Changes Induced by a Rolling Contact Bench Reproducing Wheel/Rail Contact on a Pearlitic Steel

Vincent Lafilé^{1,*} , Julie Marteau^{1,*} , Marion Risbet¹, Salima Bouvier¹ , Pierrick Merino² and Aurélien Saulot² 

¹ Sorbonne Université, Université de Technologie de Compiègne, Roberval Laboratory, Centre de Recherche de Royallieu, CS 60319, CEDEX, 60203 Compiègne, France; vincent.lafile@utc.fr (V.L.); marion.risbet@utc.fr (M.R.); salima.bouvier@utc.fr (S.B.)

² Université de Lyon, INSA-Lyon, LaMCoS UMR 5259, CEDEX, 69621 Villeurbanne, France; pierrick.merino@insa-lyon.fr (P.M.); aurelien.saulot@insa-lyon.fr (A.S.)

* Correspondence: julie.marteau@utc.fr

Abstract: Understanding the effects of wheel-rail contact on the microstructure of rails is an important issue for railway management. The impact of wheel-rail contact and surface preparation on the microstructure of rails is studied using a rolling contact bench. Microstructure changes are characterized by coupling microhardness measurements and scanning electron microscopy combined with Electron BackScattering Diffraction. This analysis led to a complete description of the sub-surface microstructure in link with the contact conditions. It was found that the use of a corroded layer on the material surface led to a considerable strain-hardening decrease. Lower surface strain-hardening was also found for sliding conditions compared to pure rolling conditions. EBSD characterizations using different indicators highlighted the importance of the scale of investigation: the use of Kernel Average Misorientation led to the identification of larger impacted depths than the Inverse Pole Figures.

Keywords: microstructure; wheel-rail contact; rolling contact bench; pearlitic steel; Electron BackScattering Diffraction



Citation: Lafilé, V.; Marteau, J.; Risbet, M.; Bouvier, S.; Merino, P.; Saulot, A. Characterization of the Microstructure Changes Induced by a Rolling Contact Bench Reproducing Wheel/Rail Contact on a Pearlitic Steel. *Metals* **2022**, *12*, 745. <https://doi.org/10.3390/met12050745>

Academic Editors: Francesca Borgioli and Zhengyi Jiang

Received: 28 February 2022

Accepted: 24 April 2022

Published: 27 April 2022

Publisher's Note: MDPI stays neutral with regard to jurisdictional claims in published maps and institutional affiliations.



Copyright: © 2022 by the authors. Licensee MDPI, Basel, Switzerland. This article is an open access article distributed under the terms and conditions of the Creative Commons Attribution (CC BY) license (<https://creativecommons.org/licenses/by/4.0/>).

1. Introduction

Efficient railway management requires a good understanding of the effects of wheel-rail contact on the microstructure of rails. One of the strategies used to examine the behavior of rail material under rolling contact is to perform an analysis of the microstructure before and after loading. At first, this analysis was often based on the use of optical microscopy combined with hardness measurements [1,2]. Then, the use of Scanning Electron Microscopy (SEM) widened [3,4], particularly to quantify the evolution of interlamellar spacing in pearlitic steels under stresses [5,6]. More recently, the use of the Electron BackScattering Diffraction (EBSD) technique was introduced, for example, to examine orientation gradients in pearlite [7] or to understand the link between hardness, crystal orientation, and cementite morphology [8]. Wen et al. [9] coupled optical microscopy, SEM, EBSD, and hardness tests to compare microstructure changes induced in two pearlitic rail steels exposed to full-scale wheel-rail contact testing. Zhao et al. [10] studied the impact of dents on the microstructure evolution of wheel/rail steel with optical microscopy, SEM, and EBSD measurements. Zhou et al. [11] investigated the performance of eutectoid and hypereutectoid rail steels by characterizing the microstructure changes caused by twin-disc testing using SEM, EBSD, and Transmission Electron Microscopy.

In spite of abundant literature on the link between the microstructure characteristics of pearlitic steels and their behavior under rolling contact remains to be thoroughly understood. This study focuses on the description of microstructure changes of R260 pearlitic steel rails induced by a rolling contact bench reproducing wheel-rail contact. In particular,

the influence of different surface preparations (as-turned *versus* corroded surface) on microstructure changes is examined, as well as the use of different loading conditions (pure rolling *versus* rolling with sliding).

2. Materials and Methods

2.1. Test Bench Conditions and Material

A special test bench called Triboring (LaMCoS, INSA Lyon, Villeurbanne, France) was used to reproduce wheel/rail contact conditions. The wheel is represented by a disk having a diameter of 70 mm, which rotates on a horizontal ring having a diameter of 2 m and a section with a 75 mm width and a 50 mm height. This ring stands for the rail. The disk and ring are independently rotated to ensure a good simulation of pure rolling contact or rolling with sliding. Both disk and ring were built from R260 steel (Table 1). Before testing a new ring, it was first turned (depth of 5 mm). A theoretical maximum pressure of 1 GPa was applied on the ring surface, and its rotation speed was 21.6 rpm. The theoretical maximum pressure was estimated based on Hertz theory: the curvature of the ring is considered infinite while the curvature of the disk is equal to 0.0353 m and 0.070 m in the x- and y-directions, respectively; Young's modulus is set to 210 GPa and Poisson's ratio to 0.27. These data led to the following values for the semi-axes of the ellipse of the contact area: 0.546 mm and 0.863 mm, thus giving a Hertzian pressure of 1 GPa.

Table 1. Chemical composition of R260 steel.

| Element | C | Si | Mn | P | S | Cr | Al |
|---------|----------|-----------|---------|--------|--------|-------|--------|
| wt % | 0.62–0.8 | 0.15–0.58 | 0.7–1.2 | ≤0.025 | ≤0.025 | ≤0.15 | ≤0.004 |

A new disk was used for each test, except in one test because of intensive wear (as mentioned in Table 2). All the details can be found in [12].

Table 2. Summary of the mechanical loadings for both tested rings (AT and AT-C).

| Ring | Test | Loading Cycle |
|------|------|--|
| AT | T1 | 1000 cycles with 0% sliding |
| | T2 | 1000 cycles with 0.5% sliding |
| | T3 | 1000 cycles with 0% sliding + 1000 cycles with 0.5% sliding |
| AT-C | T1 | 1000 cycles with 0% sliding |
| | T2 | 1000 cycles with 0.5% sliding |
| | T3 | 2000 cycles with 0.5% sliding + 1000 cycles with 0.5% sliding ¹ |

¹ A change of disk was performed after 2000 cycles because of intensive wear.

Two surface conditions for the disk/ring system were tested: either the ring was tested as turned (AT) with a slight ethanol cleaning, or a second step was added by slightly corroding the disk and ring surfaces (AT-C). The corrosion of the ring was generated by spraying the surface with water every 24 h for three days, whereas the disk was placed in water for 24 h. It led to a uniform attack. The surfaces were lightly cleaned to remove any detaching scale. An optical image of the obtained corrosion is shown in Figure 1.

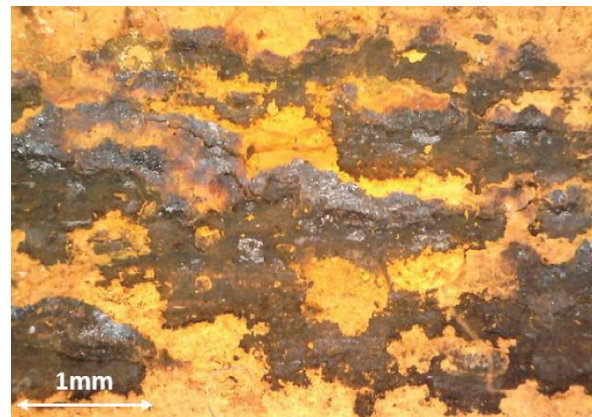
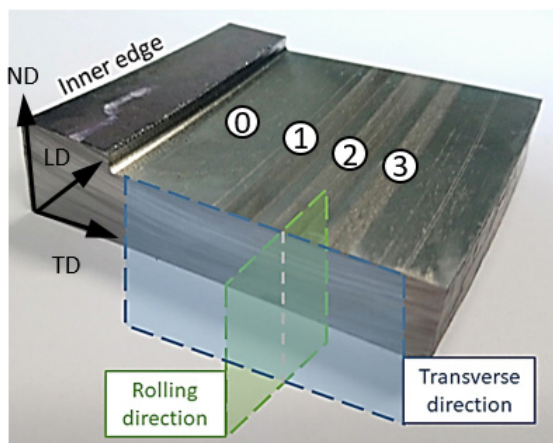


Figure 1. Optical image of the corroded surface of ring AT-C.

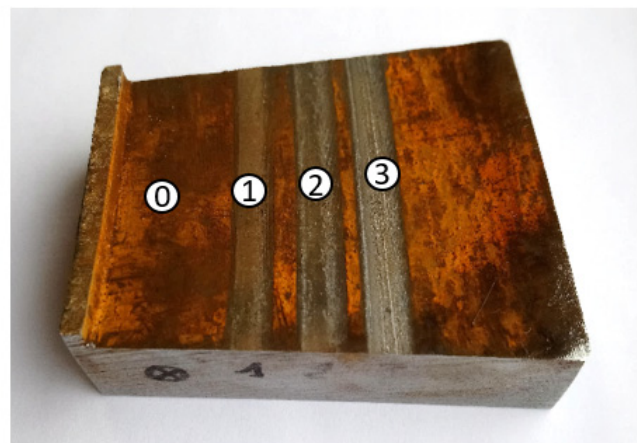
Each ring underwent three different mechanical loadings, as presented in Table 2. In the following sections, the use of T0 will designate a non-deformed part of the ring.

2.2. Microstructure Analysis and Microhardness

Several samples were cut from the R260 rings after testing, either with a surface parallel to the rolling direction (longitudinal section) or with a surface perpendicular to the rolling direction (transverse section), as shown in Figure 2. The specimens were polished using successive abrasive papers (from P80 to P4000) and then a diamond solution (3 μm , 1 μm). For EBSD measurements, an additional polishing step using colloidal silica suspensions was added.



(a)



(b)

Figure 2. Images of parts of (a) Ring AT (b) Ring AT-C, with the different directions of observation and track numbers (0 stands for the non-deformed part).

Microstructure characterizations were performed with a field emission gun-scanning electron microscope (SigmaTM, Zeiss, Oberkochen, Germany) equipped with an Electron BackScattering Diffraction (EBSD) detector (Optiplex 7040, Nordif, Trondheim, Norway). An accelerating voltage of 25 kV, a tilt of 70°, a working distance of 20 mm, and a step of 0.1 μm were used for the EBSD measurements. This step size that was chosen was about twice as inferior to the mean interlamellar spacing of the as-received pearlitic microstructure to ensure the validity of the Kernel Average Misorientation results [13]. Three measurements were performed for each test and each study direction (with a space of approximately 0.5 mm between the measurements).

Interlamellar spacing was determined by an intercept method and was computed using the ImageJ software. The interlamellar spacing is equal to the measured length divided by the number of intercepted cementite lamellae minus one. For each depth, from 10 to 15 measurements were performed.

For microhardness determination (LECO M-400 microhardness tester, LECO, St Joseph, MI, USA), a Vickers indenter was used with either a load of 100 gf ($HV_{0.1}$) or 500 gf ($HV_{0.5}$). Each indentation point in the following results corresponds to the median (and standard deviation) of three tests.

3. Results

3.1. Ring AT

First, optical observations were performed on cross-sections in the transverse direction to detect cracking. The largest crack was observed for T1 (rolling with no sliding): its length was equal to 56 μm , and it reached a depth of 6 μm . However, globally, the number of significant cracks (i.e., with a length larger than 30 μm) was found to be low, as only two to five cracks were observed for each track. It is important to underline that the use of the term ‘crack’ does not presume to describe the underlying phenomenon. The crack may be caused by a local brittle fracture or may be the result of third body flow. As illustrated in Figure 2, each track underwent measurable wear and thus a loss of material.

Then, the effects of the different loadings were investigated using microhardness measurements. The microhardness was assessed at the surface of the tracks along their width (Figure 3a) and on cross-sections to follow the evolution of hardness along the depth (Figure 3b). A larger load (500 gf) was chosen for surface testing because of the roughened state of the tracks. In Figure 3a, a global increase in the microhardness compared to the reference (T0) can be observed, whatever the test conditions. Even if the values tend to be scattered because of local roughness, the microhardness values are sensitively higher for T1 than for the other conditions. Rolling with no sliding thus seems to cause higher surface strain-hardening than rolling with sliding. The microhardness profiles performed along the depth (Figure 3b) show an increase between the surface and a depth of approximately 150 μm , whatever the test conditions. Again, the microhardness values obtained for T1 are larger than the ones obtained for the other conditions, which show similar trends. Considering the test conditions, it seems that for T3, the addition of 1000 cycles with sliding removed the impact of the previous 1000 cycles with no sliding, maybe because of material removal. Microstructure observations were performed to try to understand the previous trends.

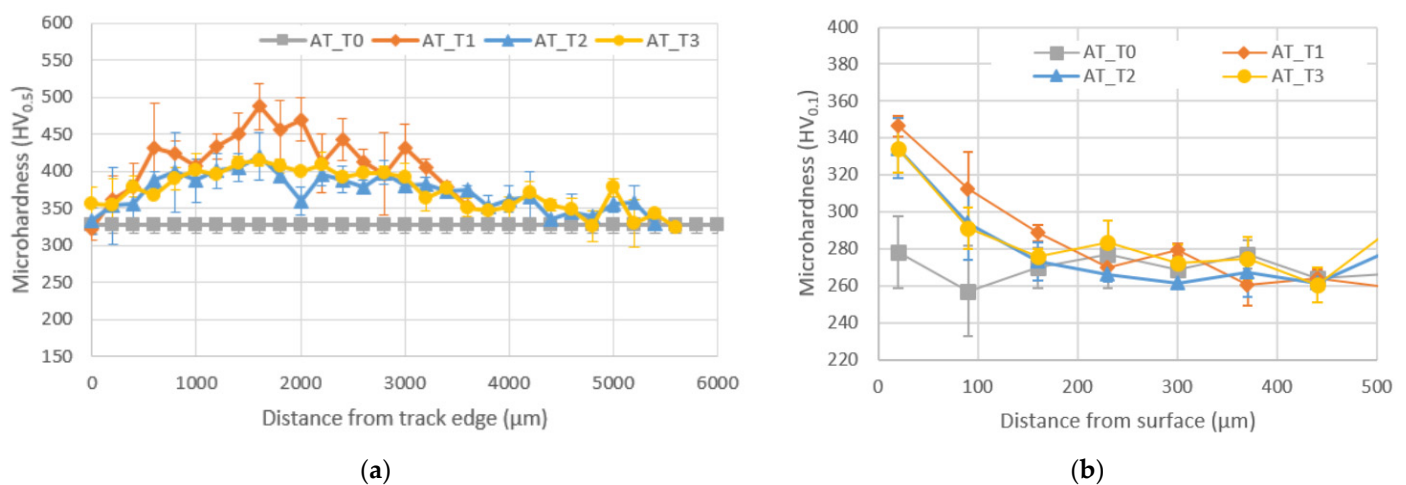


Figure 3. Microhardness results performed (a) on the surface of the tracks along their width and (b) on cross-sections for Ring AT.

The pearlitic microstructure can be observed in details in Figure 4a, while Figures A1 and A2 show larger areas of the initial microstructure. The pearlite morphology is variable: clear lamellar morphology can be observed as well as areas in which the cementite is spheroidized. This variation is further reinforced after deformation. Despite these fluctuations, interlamellar spacing in the pearlitic microstructure was measured to try to correlate its evolution with the previous microhardness trends. It was difficult to find straight lamellae groups fit for repeatable measurements. Figure 4b presents the median and standard deviations of the interlamellar spacing computed at different distances from the surface using an SEM image. Slightly lower values of the interlamellar spacing were obtained in the first 10 μm for all the tested conditions. However, the variability is too high to ensure data robustness.

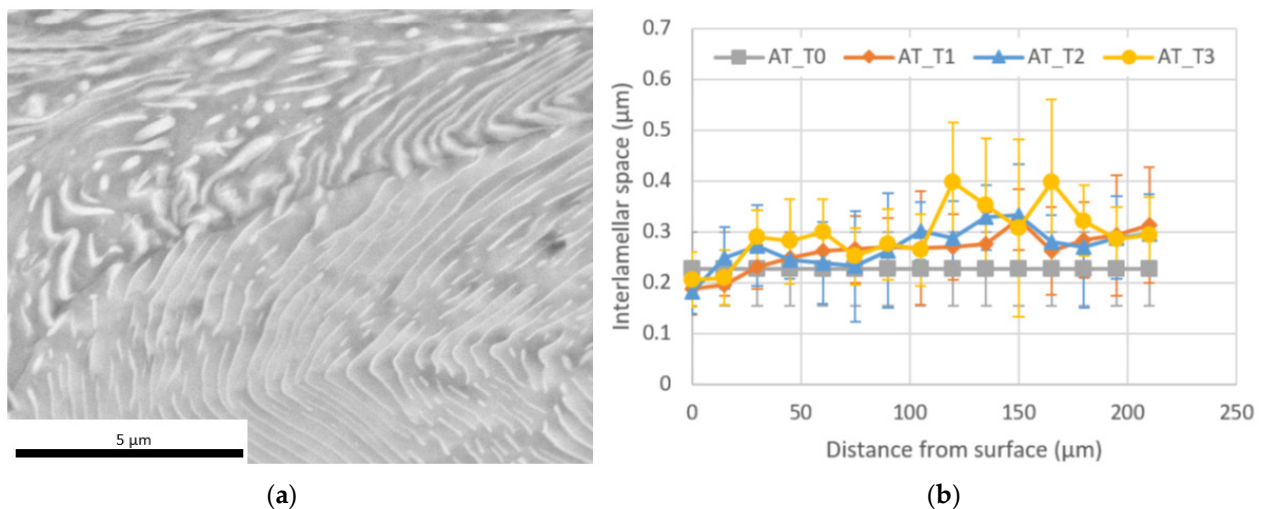


Figure 4. (a) SEM image of the pearlitic microstructure (AT-T0) and (b) interlamellar spacing for Ring AT.

By using the EBSD measurements, inverse pole figure (IPF) maps of ferrite were coupled with Index Quality (IQ) maps to visualize orientations and the underlying microstructures (as cementite is not indexed, it appears in black in the IQ map). Kernel Average Misorientation (KAM) maps were also computed to observe the evolution of local grain misorientation with deformation. Both types of maps are shown for all the tested conditions in Figure 5. For the non-deformed state (T0), the first 5–10 μm suffer from poor indexation. It leads to the appearance of very small grains on the maps that are not significant. This poor indexation is probably caused by surface turning. According to previous works [9,13], the nodules and colonies can be clearly identified by combining the map data: high-angle misorientations (KAM larger than 15°) surround the nodules while KAM around 5° tend to underline the colony boundaries. The maps corresponding to the different tested conditions are all characterized by deformed microstructures: a clear flattening and tilt of the microstructure components can be perceived, as well as fragmentation. For T1, the first 15 μm are strongly affected by a low indexation, thus preventing a robust conclusion. However, there seems to be a heavy fragmentation of the microstructure. Then, from a depth of 15 μm to 30 μm , nodule boundaries are lost, and the pearlite colonies are fragmented, as confirmed by the KAM map in which there is a high density of KAM angles comprised between 2 and 65° . After 30 μm , there is a gradual decrease in the density of KAM angles: nodules are still deformed but are now clearly visible. Larger EBSD maps were performed to determine the impacted depth. An example is given in Figure 6. Even if the IPF shows a microstructure similar to the non-deformed state around a depth of 50–60 μm , the KAM maps showed that KAM distribution similar to the non-deformed state was retrieved from a depth of around 100 μm . The near-surface of T2 is less affected by low indexation than T1, and the microstructure is globally less impacted by the deformation.

From 5 to 15 μm , the observed microstructure is less fragmented than T1, and KAM angles are mainly comprised between 2 and 5°. Then, around 25–30 μm of depth, nodules can be easily identified even if the density of KAM angles between 2 and 5° remains high. KAM distribution similar to the non-deformed state is retrieved for a depth of around 80 μm . Finally, T3 presents a structuration similar to T1 but on a smaller depth: using the IPF map, the nodules seem to be similar to the non-deformed state from a depth of 30 μm . The KAM map shows a distribution similar to the non-deformed state from a depth of around 70–80 μm .

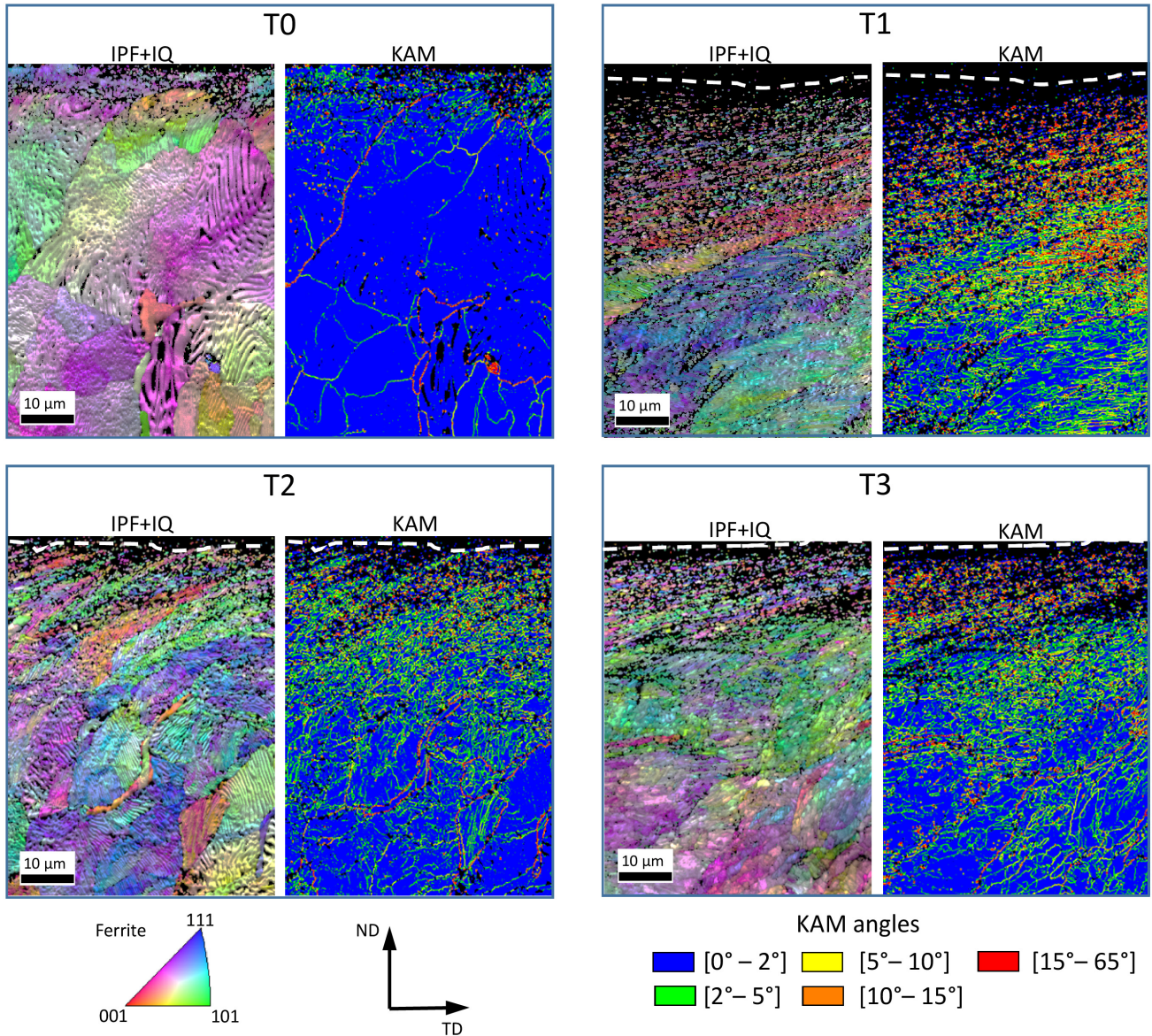


Figure 5. IPF map with IQ and KAM maps for the non-deformed state (T0) and the different testing conditions (T1, T2, T3), for Ring AT. The measurements were performed along the transverse direction.

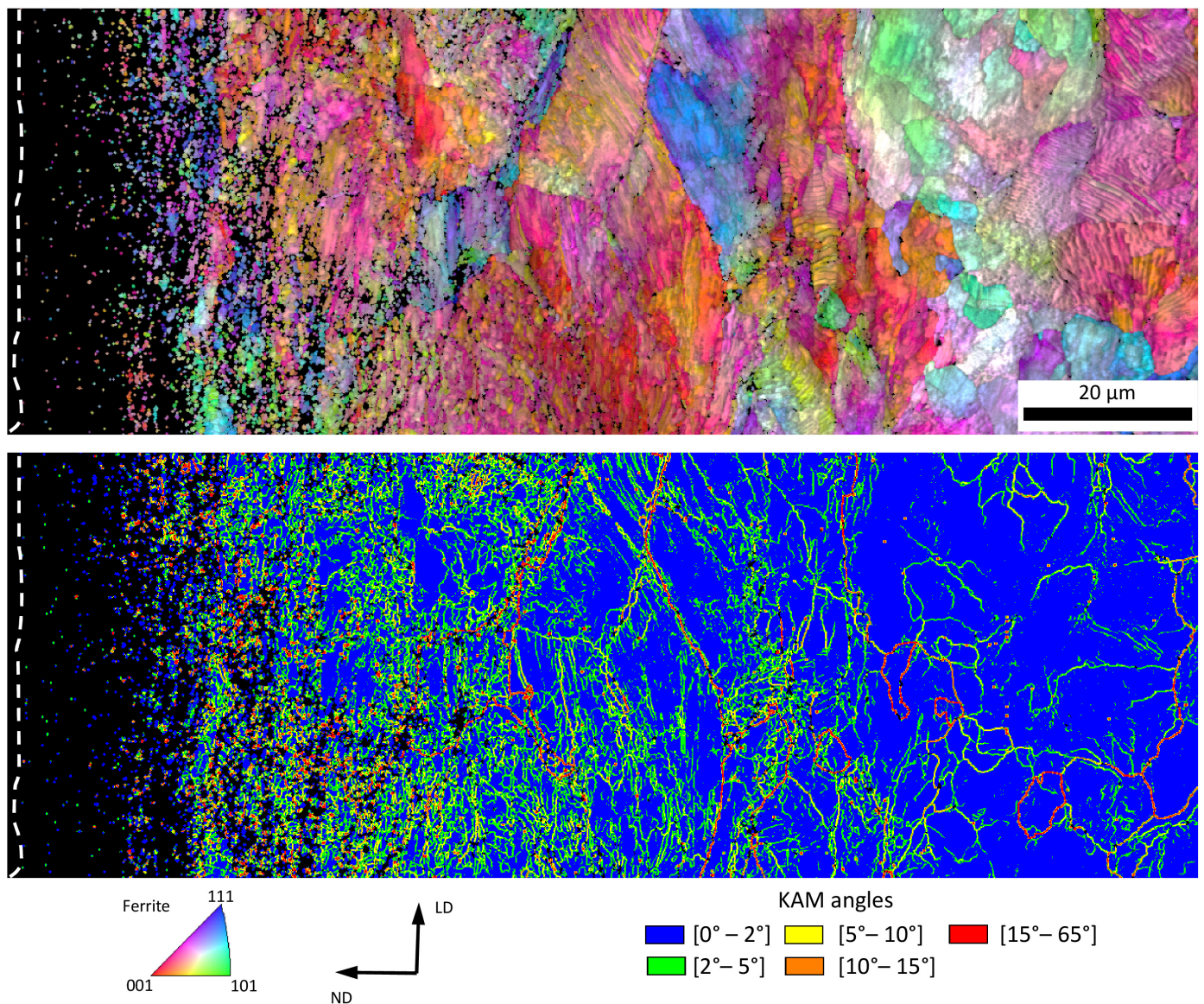


Figure 6. IPF map with IQ and KAM maps of a larger region for AT_T1 (as-turned with 1000 cycles with no sliding). The measurements were performed along the longitudinal direction.

Similar observations were made in the longitudinal direction for all the tested conditions. Examples of IPF with IQ maps and KAM maps are shown in Figure A3.

As the EBSD indexation is low near the surface, SEM pictures are provided for a better description of the microstructure (Figure 7). For AT_T0, the pearlite microstructure is lost for the first micrometers. It seems to be heavily by turning. Among all the tested conditions, T2 seems to present the lower sub-surface modification: the lamellar structure of pearlite can be detected from 2 μm below the surface. On the contrary, the lamellar microstructure is completely lost for T1 and T3 for the first 5 μm .

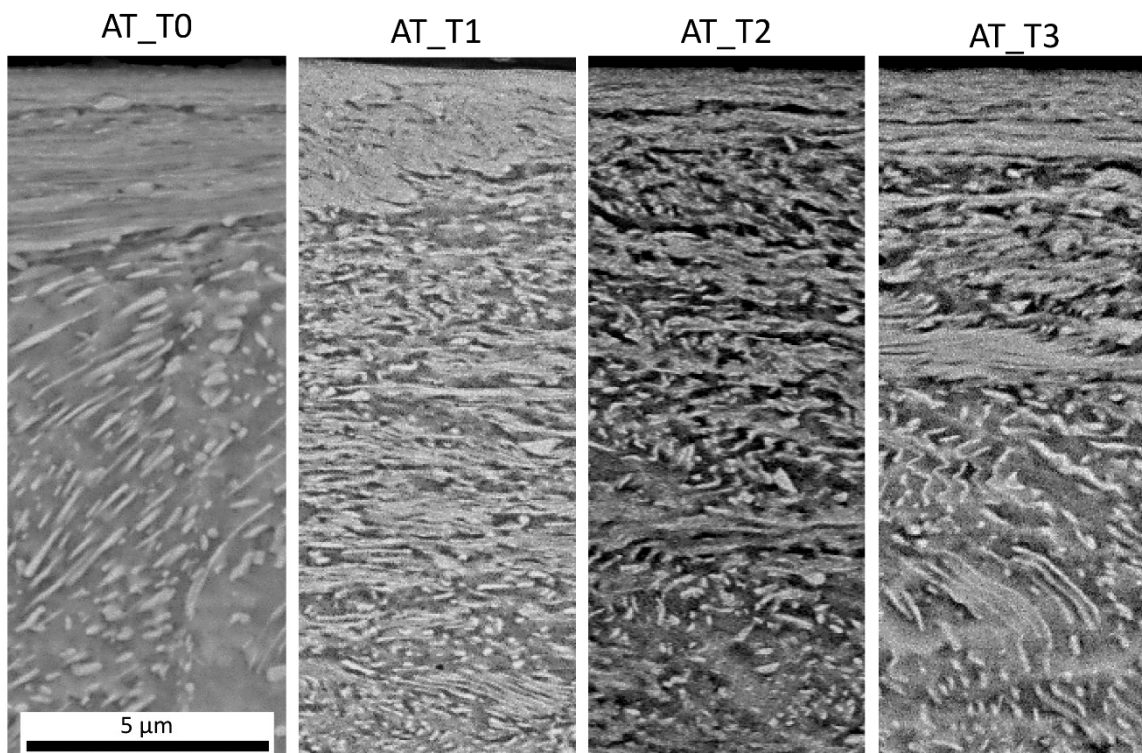


Figure 7. SEM images of the near-surface in the transverse direction, for all the tracks of Ring AT.

3.2. Ring AT-C

Similar analyses were performed on Ring AT-C to examine the effect of the corroded layer on the material deformation. The optical observations performed on cross-sections in the transverse direction showed only a few cracks for T1 and T2 (only five cracks with a length larger than $30\ \mu\text{m}$). On the opposite, for T3, 19 cracks larger than $30\ \mu\text{m}$ were found, with the largest having a length of $125\ \mu\text{m}$ and a depth of $12\ \mu\text{m}$. Cracks tend to develop in a direction parallel to the surface, probably leading to chipping.

Figure 8 shows the microhardness results obtained on the surface, along the track widths, and on the cross-sections. Despite the scatter of the values caused by roughness, a clear increase in microhardness can be identified on the surface of all the tracks (Figure 8a). Similar trends are obtained for T1 and T2, whereas larger microhardness values are obtained for T3: the maximum values are around $400\ \text{HV}_{0.5}$ for T1 and T2, while the maximum value is equal to $500\ \text{HV}_{0.5}$ for T3. As for the microhardness profiles performed on the cross-sections (Figure 8b), there is an increase in microhardness values from the surface to a depth of approximately $100\ \mu\text{m}$. Again, the largest values are obtained for T3 ($370\ \text{HV}_{0.1}$ against $290\text{--}310\ \text{HV}_{0.1}$ for the other tests).

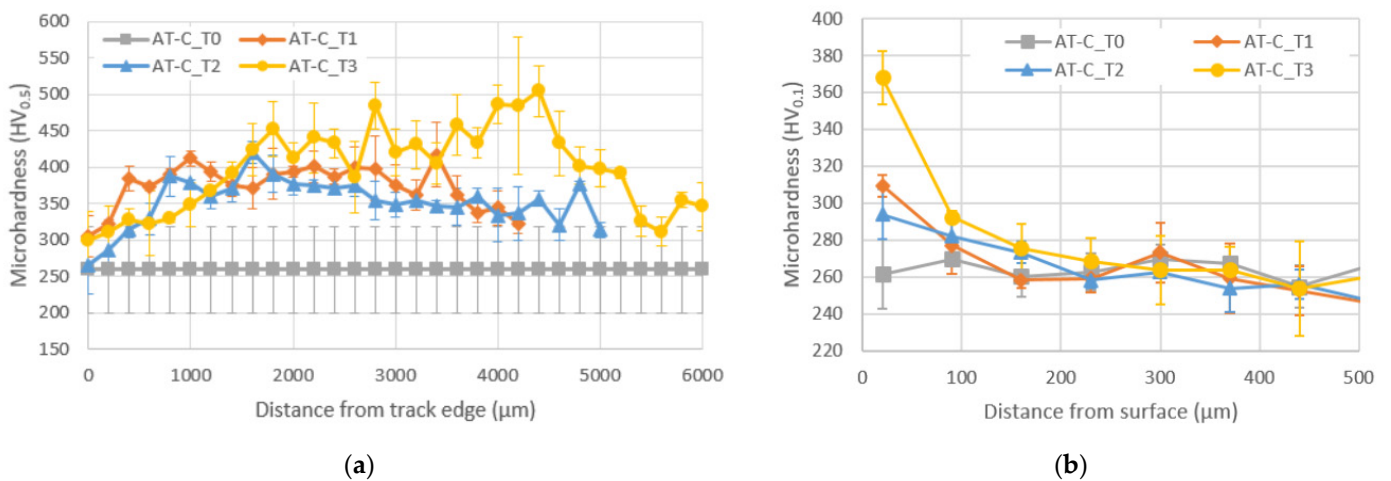


Figure 8. Microhardness results performed (a) on the surface of the tracks along their width and (b) on cross-sections for Ring AT-C.

Figure 8 can also be compared with Figure 3 to assess the possible impact of corrosion on the surface hardness of the specimen. It seems that larger surface microhardness values are found for AT_T0 compared to AT-C_T0 (328 ± 10 HV_{0.5} versus 259 ± 59 HV_{0.5} at the surface or 278 ± 20 HV_{0.1} versus 262 ± 19 HV_{0.1} for a 20 μm depth). It could be assumed that the corrosion layer tends to decrease the surface microhardness locally. However, for AT_T0, larger microhardness values are obtained on the surface compared to a depth of 20 μm, while similar values are obtained for AT-C_T0 on the surface compared to a depth of 20 μm or even larger depths. As different loads were used, the values cannot be directly compared but clearly indicate a stronger microhardness gradient in AT_T0, thus confirming a possible strain-hardening caused by surface turning as suggested in Section 3.1.

The initial microstructure of Ring AT-C can be observed in Figures A1 and A2. Again, the pearlite morphology is variable: the microstructure is similar to the one observed for Ring AT, except that some areas of small sizes containing only ferrite can also be observed. Thus, the difference in interlamellar spacing between the non-deformed conditions and the tests was difficult to assess because of the large data scatter (Figure 9). However, a significant decrease for T1, T2, and T3 can be perceived for the first 15 μm (with values between 150–200 nm against 300 nm for the reference).

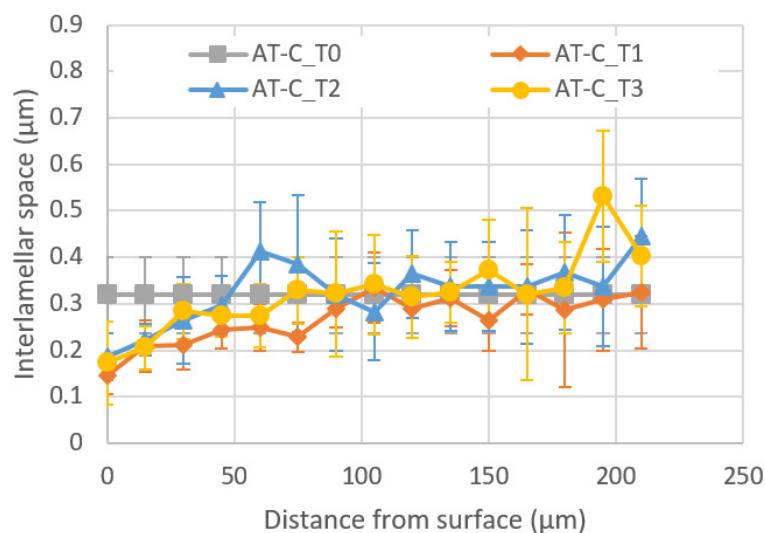


Figure 9. Evolution of interlamellar spacing with depth for Ring AT-C.

Figure 10 gathers the IPF maps with IQ and KAM maps for the non-deformed state (T0) and the different testing conditions (from T1 to T3) for Ring AT-C. For T1, from the surface down to around 10–15 μm , the indexation is very low, thus preventing any robust conclusion on microstructure changes. Then, from around 15 μm to 40 μm , the nodules and colonies are first very deformed but can still be distinguished. Their shape is then progressively rounder even if the disorientations remain important. This region corresponds to a high density of KAM angles comprised between 2° and 10° . The KAM distribution is affected until a depth of 70 μm . For T2, the loss of indexation in the near-surface takes place over approximately 5 μm . Then, from 5 to 20 μm , there is first some fragmentation and then deformation of the microstructure. Compared to T1, there is a rather sharp transition in the IPF map and KAM map around 20 μm , even if the KAM distribution returns to a non-deformed state around 50 μm . For T3, low indexation takes place from the surface to a depth of around 15 μm . There seems to be some heavy fragmentation. Then, from 15 to 60 μm , fragmentation becomes less important, but the nodules are strongly deformed. KAM density is high with angles between 2° and 10° . Based on the IPF map, the affected depth seems to be around 60–70 μm . However, KAM maps only stabilize at a depth of 100 μm . Similar results were found when examining the longitudinal views. Some examples are given in Figure A4.

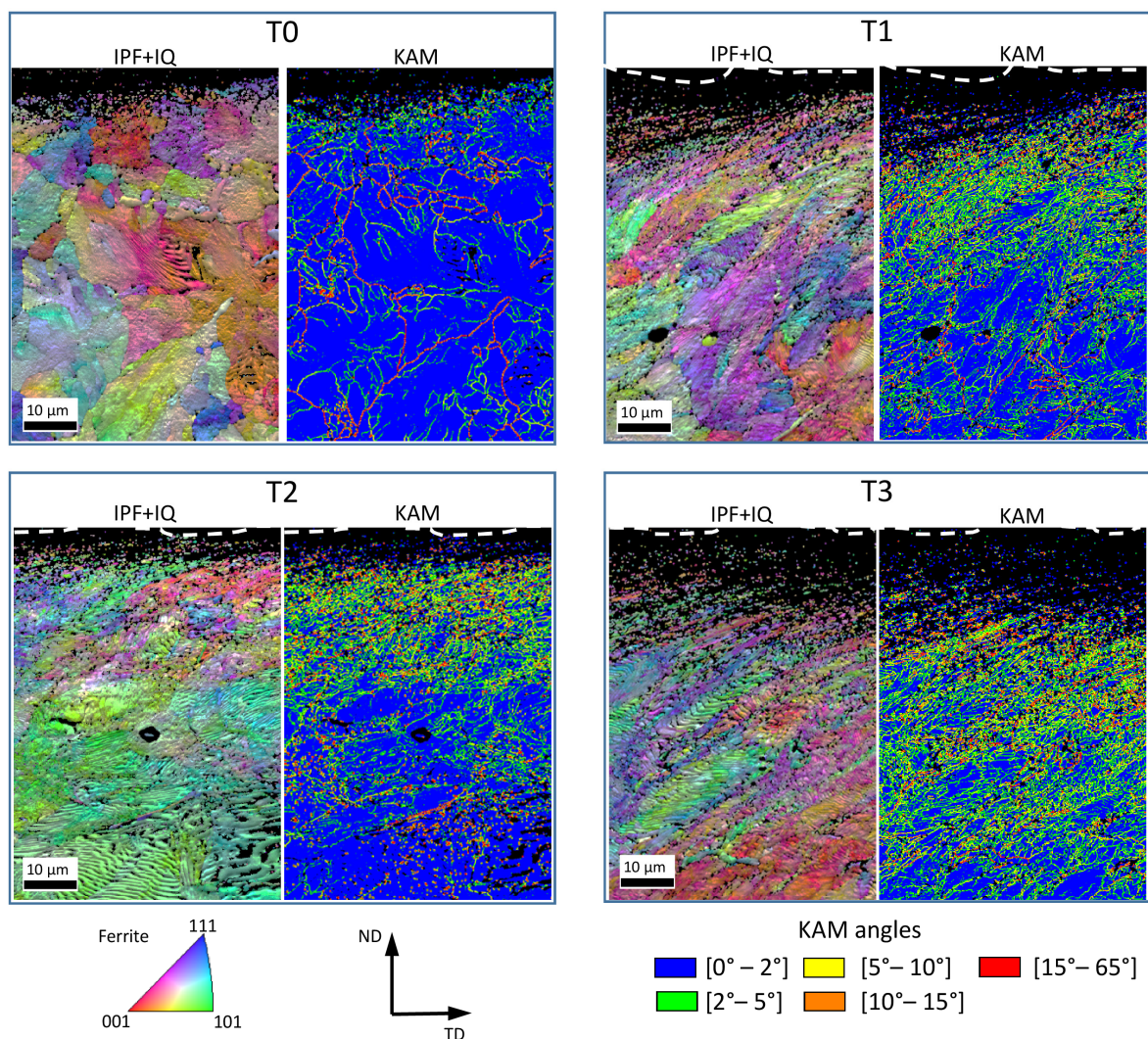


Figure 10. IPF map with IQ and KAM maps for the non-deformed state (T0) and the different testing conditions (T1, T2, T3), for Ring AT-C. The measurements were performed along the transverse direction.

Again, as the EBSD indexation is too low for the first ten micrometers to be able to describe the microstructure changes, SEM pictures were taken to illustrate the microstructure changes caused by the different test conditions (Figure 11). For T0, only the first two micrometers seem to be impacted by turning (loss of pearlite microstructure). For T1 and T2, the lamellar microstructure can be easily distinguished from 2–3 μm . On the contrary, for similar depths, for T3, broken lamellae can still be observed and can be perceived until the end of the presented cross-section.

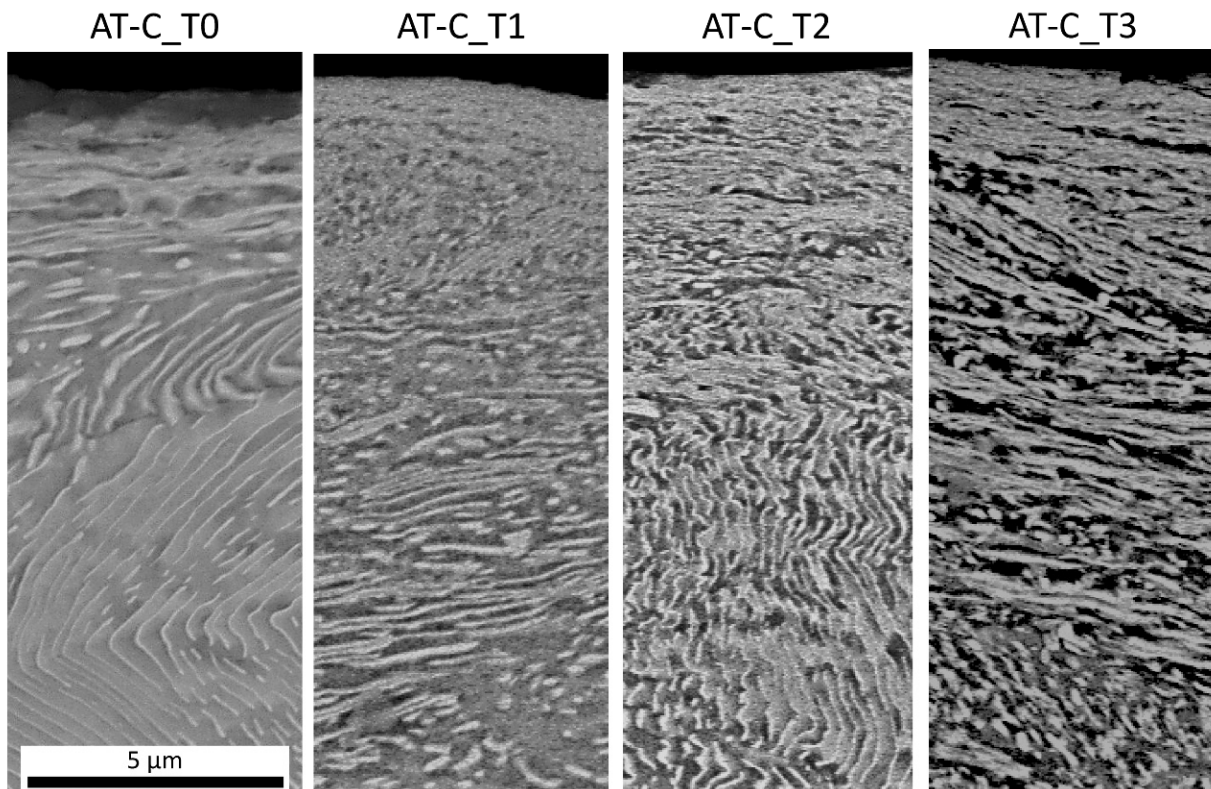


Figure 11. SEM images of the near-surface in the transverse direction, for all the tracks of Ring AT-C.

4. Discussion

Comparing the results of AT_T1 and AT_T2 enables the influence of sliding to be examined: the loading can be assimilated either to a normal stress condition (no sliding) or to a normal and shear stress condition (with sliding). The introduction of sliding causes a slight decrease in surface hardness (around 350 $\text{HV}_{0.1}$ with no sliding against 335 $\text{HV}_{0.1}$ with sliding) and the depth impacted by strain-hardening. Similarly, based on the KAM distributions, the microstructure stops being impacted at a depth of approximately 100 μm with pure rolling (no sliding) against 80 μm with sliding. AT-T3 combines a succession of 1000 cycles with pure rolling (no sliding) and then 1000 cycles with sliding. The surface hardening results are very similar to the ones obtained for AT_T2. The microstructure is also impacted at a similar depth (around 80 μm based on KAM distribution). The addition of 1000 cycles with sliding seems to have eliminated part of the effects of the 1000-cycle loading with no sliding. The introduction of sliding causes surface wear. Nevertheless, it has been shown that a rolling condition (AT_T3) generates the occurrence of a fuse layer composed of nanograins reducing later wear occurrence [12]. Through KAM investigation, this new study demonstrated that this run-in fuse layer also promotes the confinement of plastic deformation beneath the surface (100 μm for AT_T1 was reduced to 80 μm for AT_T3).

The comparison of AT_T1 and AT-C_T1 enables the impact of the corroded layer for a loading of 1000 cycles with no sliding to be examined. The introduction of a corroded

layer leads to a decrease in surface microhardness from 350 HV_{0.1} to 310 HV_{0.1}, as well as a decrease in the impacted depth. The material is thus not effectively strain-hardened when the corroded layer is present. These changes are also reflected in the microstructure modifications. The observations of the KAM distributions led to the identification of an impacted depth of around 100 µm without the corroded layer while it is around 70 µm with the corroded layer. Globally, the microstructure was more heavily fragmented and deformed when the corroded layer was omitted. This gain can also be noted with the other two tested conditions: the introduction of sliding with a corroded layer (AT-C_T2) leads to a decrease in surface hardening and the impacted depth. The loading of 3000 cycles with sliding with a corroded layer (AT-C_T3) gives the largest surface hardening (370 HV_{0.1}), but the results remain close to the ones obtained with the 1000-cycle loading with no sliding (AT_T1). However, the comparison of the KAM distributions indicates that a higher density is obtained with the no-sliding conditions with higher values of angles. This corroded layer seems to play the role of an additional fuse layer, which enables the subsurface pearlitic microstructure to transform into a nanograin substructure, which is at first protected from wear by the oxide layer. It has been shown that this phenomenon is accompanied by mechanical white etching layer formation [12].

5. Conclusions

This study examined the impact of different surface preparations and loading conditions on the sub-surface mechanical properties and microstructure. Hardness measurements showed that lower surface strain-hardening is caused when using a corroded layer instead of a bare and cleaned as-turned surface. Smaller surface strain-hardening was also observed for sliding conditions compared to pure rolling.

These changes in sub-surface mechanical properties were confirmed by EBSD analyses of the microstructure. The use of different maps (inverse pole figure with index quality versus kernel average misorientation) highlighted the importance of the scale of investigation: different conclusions could be made on the impacted depth depending on the chosen indicator. The KAM maps revealed a larger impacted depth than the observation of IPF maps.

Author Contributions: Conceptualization, A.S. and M.R.; methodology, V.L., P.M., A.S., M.R., S.B. and J.M.; validation, V.L., A.S., M.R., S.B. and J.M.; formal analysis, V.L., M.R., S.B. and J.M.; investigation, V.L., P.M., A.S., M.R., S.B. and J.M.; resources, V.L., A.S., M.R., S.B. and J.M.; data curation, V.L. and J.M.; writing—original draft preparation, V.L. and J.M.; writing—review and editing, V.L., A.S., M.R., S.B. and J.M.; visualization, V.L. and J.M.; supervision, A.S., S.B., J.M. and M.R.; project administration, A.S. and M.R.; funding acquisition, A.S. and M.R. All authors have read and agreed to the published version of the manuscript.

Funding: This research was funded by RATP (Régie Autonome des Transports Parisiens).

Institutional Review Board Statement: Not applicable.

Informed Consent Statement: Not applicable.

Data Availability Statement: Data available on request due to restrictions.

Acknowledgments: The authors would like to thank Eric Vittecoq (Hepia Geneva) for the design of the test bench and also Xavier Quost, Samuel Simon, Pierre Boutet from RATP (Paris Public Transport) as well as Frédéric Fau and François Cristofari from British Steel for providing the steel samples and funding of this study.

Conflicts of Interest: The authors declare no conflict of interest.

Appendix A

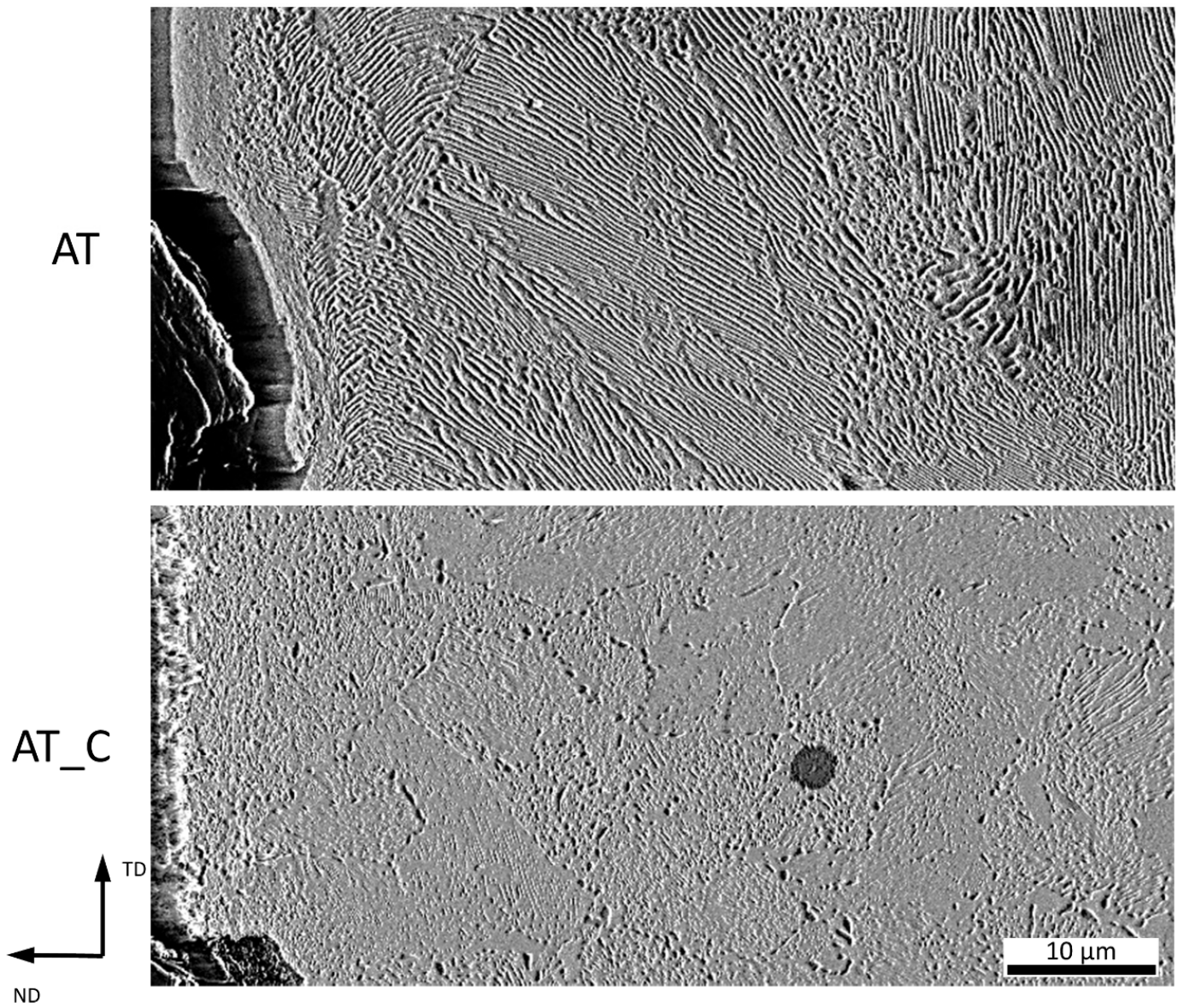


Figure A1. SEM images for the non-deformed state (T0) for Ring AT and Ring AT_C. The measurements were performed along the transverse direction.

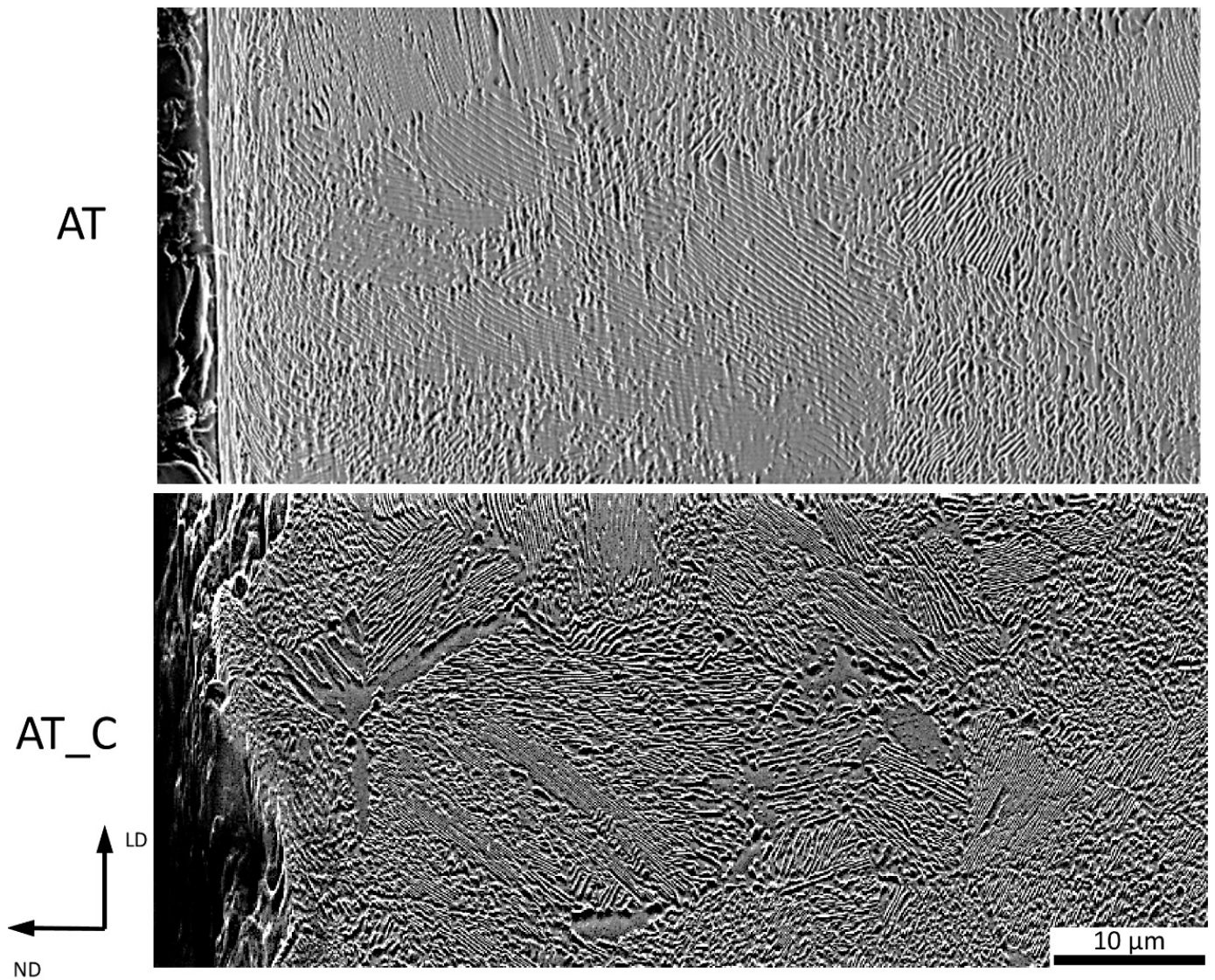


Figure A2. SEM images for the non-deformed state (T0) for Ring AT and Ring AT_C. The measurements were performed along the longitudinal direction.

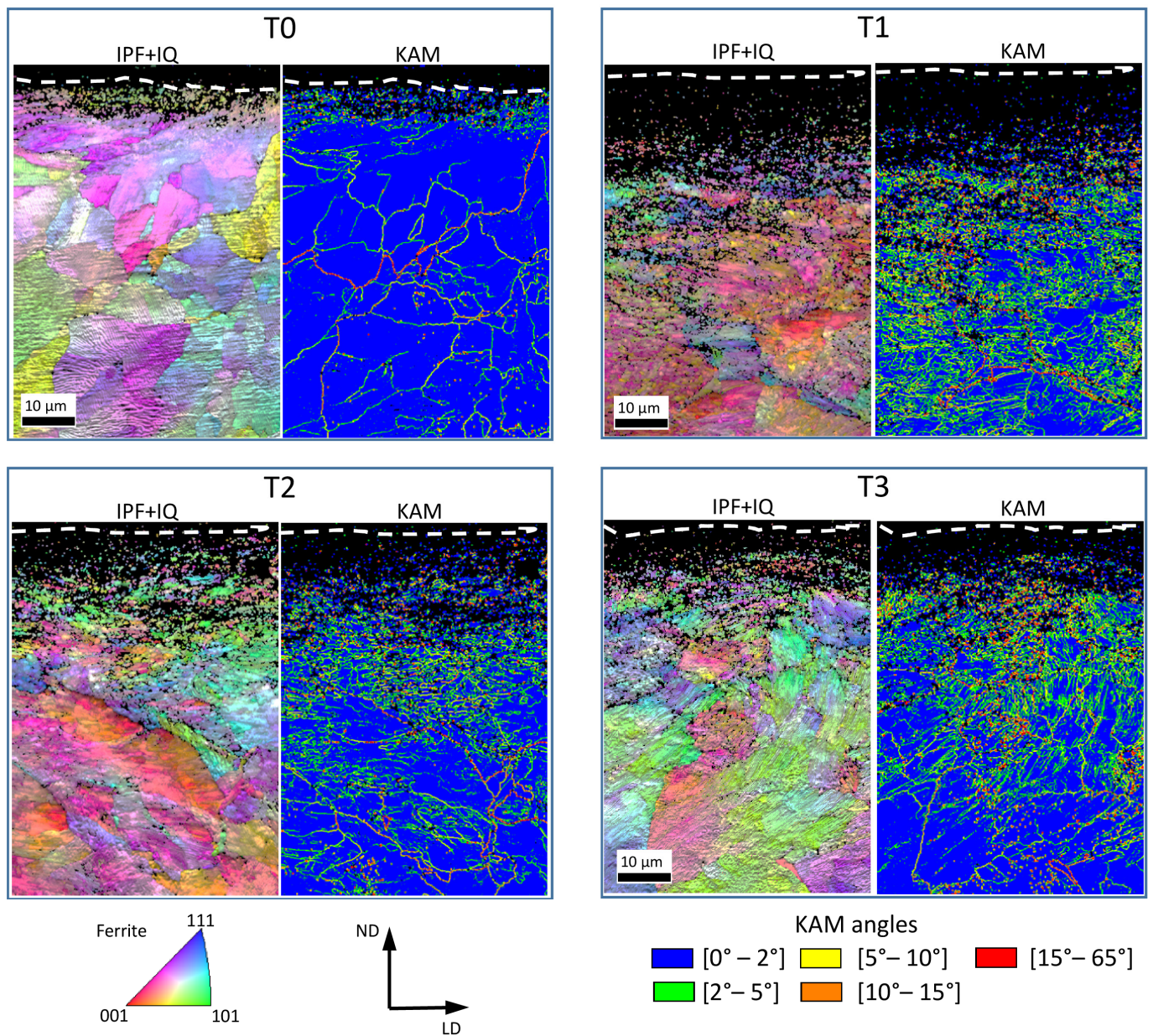


Figure A3. IPF map with IQ and KAM maps for the non-deformed state (T0) and the different testing conditions (T1, T2, T3), for Ring AT. The measurements were performed along the longitudinal direction.

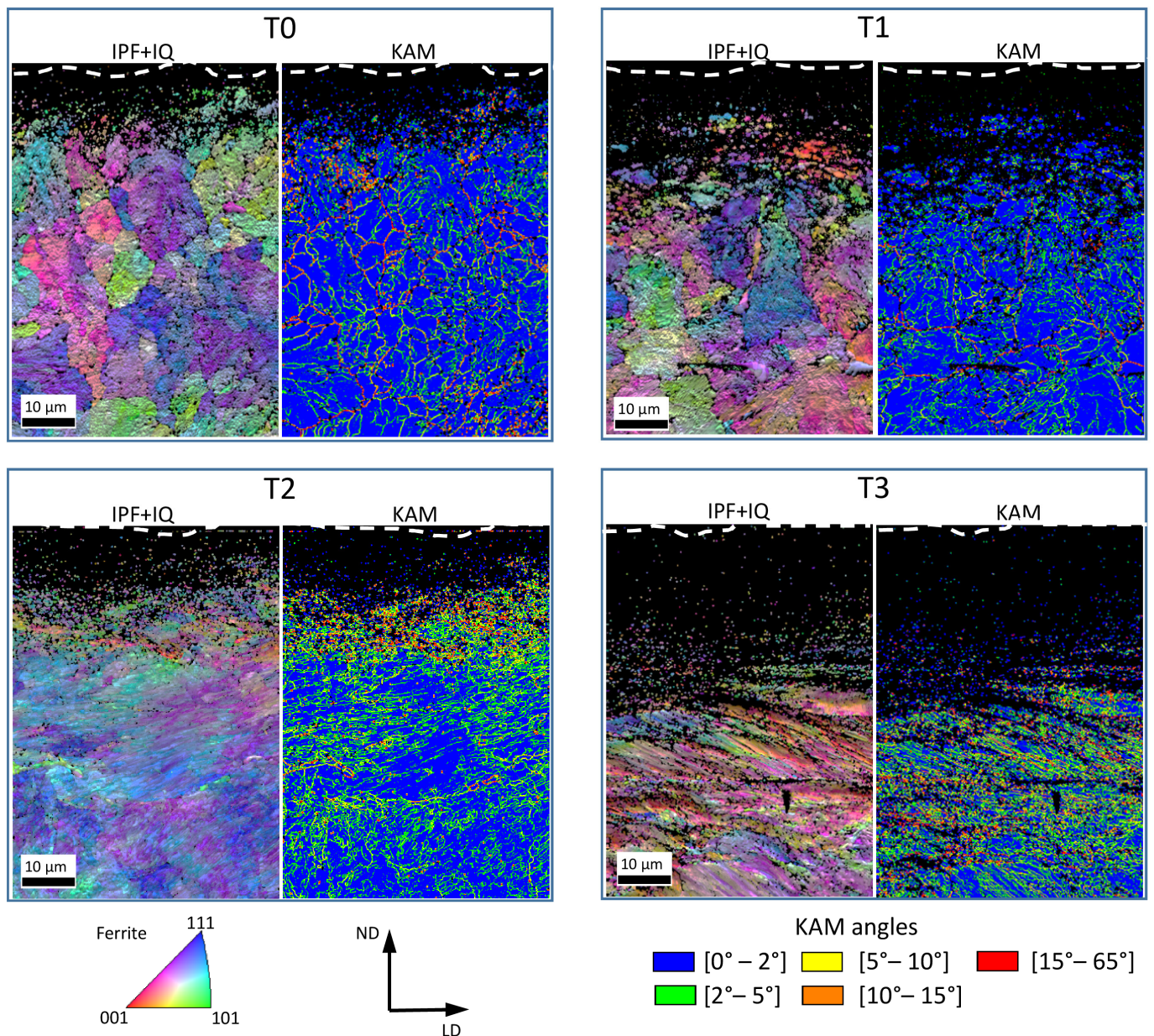


Figure A4. IPF map with IQ and KAM maps for the non-deformed state (T0) and the different testing conditions (T1, T2, T3), for Ring AT-C. The measurements were performed along the longitudinal direction.

References

1. Alwahdi, F.A.M.; Kapoor, A.; Franklin, F.J. Subsurface microstructural analysis and mechanical properties of pearlitic rail steels in service. *Wear* **2013**, *302*, 1453–1460. [[CrossRef](#)]
2. Zhao, X.J.; Guo, J.; Wang, H.Y.; Wen, Z.F.; Liu, Q.Y.; Zhao, G.T.; Wang, W.J. Effects of decarburization on the wear resistance and damage mechanisms of rail steels subject to contact fatigue. *Wear* **2016**, *364–365*, 130–143. [[CrossRef](#)]
3. Garnham, J.E.; Davis, C.L. The role of deformed rail microstructure on rolling contact fatigue initiation. *Wear* **2008**, *265*, 1363–1372. [[CrossRef](#)]
4. Maya-Johnson, S.; Ramirez, A.J.; Toro, A. Fatigue crack growth rate of two pearlitic rail steels. *Eng. Fract. Mech.* **2015**, *138*, 63–72. [[CrossRef](#)]
5. Athukorala, A.C.; De Pellegrin, D.V.; Kourousis, K.I. Characterisation of head-hardened rail steel in terms of cyclic plasticity response and microstructure for improved material modelling. *Wear* **2016**, *366–367*, 416–424. [[CrossRef](#)]
6. Wetscher, F.; Stock, R.; Pippan, R. Changes in the mechanical properties of a pearlitic steel due to large shear deformation. *Mater. Sci. Eng. A* **2007**, *445–446*, 237–243. [[CrossRef](#)]

7. Takahashi, T.; Ponge, D.; Raabe, D. Investigation of Orientation Gradients in Pearlite in Hypoeutectoid Steel by use of Orientation Imaging Microscopy. *Steel Res. Int.* **2007**, *78*, 38–44. [[CrossRef](#)]
8. Debehets, J.; Tacq, J.; Favache, A.; Jacques, P.; Seo, J.W.; Verlinden, B.; Seefeldt, M. Analysis of the variation in nanohardness of pearlitic steel: Influence of the interplay between ferrite crystal orientation and cementite morphology. *Mater. Sci. Eng. A* **2014**, *616*, 99–106. [[CrossRef](#)]
9. Wen, J.; Marteau, J.; Bouvier, S.; Risbet, M.; Cristofari, F.; Secordel, P. Comparison of microstructure changes induced in two pearlitic rail steels subjected to a full-scale wheel/rail contact rig test. *Wear* **2020**, *456–457*, 203354. [[CrossRef](#)]
10. Zhao, X.J.; Guo, J.; Liu, Q.Y.; Butini, E.; Marini, L.; Meli, E.; Rindi, A.; Wang, W.J. Effect of spherical dents on microstructure evolution and rolling contact fatigue of wheel/rail materials. *Tribol. Int.* **2018**, *127*, 520–532. [[CrossRef](#)]
11. Zhou, L.; Bai, W.; Han, Z.; Wang, W.; Hu, Y.; Ding, H.; Lewis, R.; Meli, E.; Liu, Q.; Guo, J. Comparison of the damage and microstructure evolution of eutectoid and hypereutectoid rail steels under a rolling-sliding contact. *Wear* **2022**, *492–493*, 204233. [[CrossRef](#)]
12. Merino, P.; Cazottes, S.; Lafilé, V.; Risbet, M.; Saulot, A.; Bouvier, S.; Marteau, J.; Berthier, Y. An attempt to generate mechanical white etching layer on rail surface on a new rolling contact test bench. *Wear* **2021**, *482–483*, 203945. [[CrossRef](#)]
13. Dylewski, B.; Risbet, M.; Bouvier, S. The tridimensional gradient of microstructure in worn rails—Experimental characterization of plastic deformation accumulated by RCF. *Wear* **2017**, *392–393*, 50–59. [[CrossRef](#)]